The Interplay of Symmetry and Scattering Phase in Second Harmonic Generation from Gold Nanoantennas

Sylvain D. Gennaro,[†] Mohsen Rahmani,[†] Vincenzo Giannini,[†] Heykel Aouani,[†] Themistoklis P. H. Sidiropoulos,[†] Miguel Navarro-Cía,[‡] Stefan A. Maier,[†] and Rupert F. Oulton[*,†]

[†]The Blackett Laboratory, Department of Physics, Imperial College London, London SW7 2AZ, United Kingdom
[‡]School of Physics and Astronomy, University of Birmingham, Birmingham B15 2TT, United Kingdom

ⓢ *Supporting Information*

ABSTRACT: Nonlinear phenomena are central to modern photonics but, being inherently weak, typically require gradual accumulation over several millimeters. For example, second harmonic generation (SHG) is typically achieved in thick transparent nonlinear crystals by phase-matching energy exchange between light at initial, ω, and final, 2ω, frequencies. Recently, metamaterials imbued with artificial nonlinearity from their constituent nanoantennas have generated excitement by opening the possibility of wavelength-scale nonlinear optics. However, the selection rules of SHG typically prevent dipole emission from simple nanoantennas, which has led to much discussion concerning the best geometries, for example, those breaking centro-symmetry or incorporating resonances at multiple harmonics. In this work, we explore the use of both nanoantenna symmetry and multiple harmonics to control the strength, polarization and radiation pattern of SHG from a variety of antenna configurations incorporating simple resonant elements tuned to light at both ω and 2ω. We use a microscopic description of the scattering strength and phases of these constituent particles, determined by their relative positions, to accurately predict the SHG radiation observed in our experiments. We find that the 2ω particles radiate dipolar SHG by near-field coupling to the ω particle, which radiates SHG as a quadrupole. Consequently, strong linearly polarized dipolar SHG is only possible for noncentro-symmetric antennas that also minimize interference between their dipolar and quadrupolar responses. Metamaterials with such intra-antenna phase and polarization control could enable compact nonlinear photonic nanotechnologies.

KEYWORDS: *Nonlinear optics, second harmonic generation, nanoantennas, plasmonics, metamaerials*
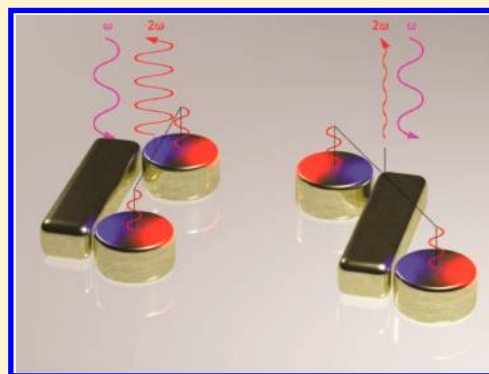
A recurring theme in optics and photonics is the ability of metal nanostructures to imbue artificial materials with new functions. Metallic nanoantennas,[1] so-called meta-atoms, are the building blocks of such metamaterials that boast unusual linear[2,3] and nonlinear[4−6] characteristics. Recently, nonlinear metamaterials have generated considerable excitement; while nonlinear effects in natural materials must gradually accumulate weak nonlinearity across macroscopic crystal dimensions, a small volume of metamaterial,[7,8] and even isolated nanoantennas,[9−12] can create a surprisingly strong effect. This capability stems from additional nanoscopic degrees of freedom that include couplings between the constituent nanoparticles within nanoantennas or between nanoantennas and material resonances.[7−9,13,14] Moreover, metamaterials do not necessarily follow the convention that the strength of nonlinearity in certain materials stems from their linear properties.[15,16] This suggests a departure from conventional physical limitations in nonlinear optics. Metamaterials with tailored nonlinear responses look set to provide exceptional flexibility in applications such as super-resolution imaging,[17] efficient frequency conversion,[18] optical switching, and coherent optical control at the nanoscale.[19,20]

Second harmonic generation (SHG) from metal nanoantennas is a particularly interesting effect as metals belong to a class of materials with symmetry-forbidden even order nonlinearity. Although it has been known for some time that the broken symmetry of a metal's surface produces a second order nonlinear response, resonant metal nanoparticles can significantly enhance SHG using a number of additional techniques, for example, exploiting enhanced absorption at Fano resonances;[21−23] breaking the symmetry with the nano-antenna's own geometry;[24,25] in-plane external phase control of nanoantenna arrays to direct and focus SHG;[7,8] and designing nanoantennas with coupled nanoparticles that are resonant at both pump and SHG frequencies.[11,14,25−28]

In this paper, we examine the importance of the nanoantenna configuration on SHG's strength, polarization, and emission pattern. Each nanoantenna in our investigation consists of a single ω-particle (bar) and a number of 2ω-particles (discs) tuned to the pump and second harmonic frequencies,

respectively. Using these constituent particles in a range of configurations, we show how the activation and deactivation of an antenna's dipole SHG emission can be understood in terms of the interference of the dipole and quadrupole sources of the antenna. For example, the location of each 2ω-particle relative to the ω-particle determines its radiation phase at the second harmonic frequency. When positioned in a noncentro-symmetric arrangement, multiple 2ω-particles constructively interfere to generate a linearly polarized and "bright" dipole SHG emission pattern (left nanoantenna in Figure 1). However, a centro-
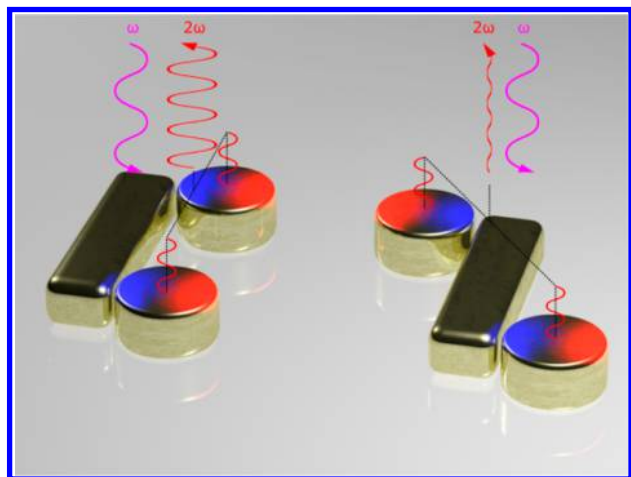
Figure 1. Illustration of SHG interference in multiresonant gold nanoantennas. The image shows two of the nanoantenna configurations investigated (CIII and CIV). The nanoantennas are initially excited through a bar-shaped particle (ω-particle). The two discs (2ω-particles) in the nanoantenna on the left radiate in phase leading to bright and directional SHG. Meanwhile, the nanoantenna on the right suppresses SHG normal to the substrate surface as its 2ω-particles radiate out of phase.

symmetric configuration enforces destructive interference of the 2ω-particles to leave only a "dark" remnant of quadrupole scattering at the second harmonic frequency (right nanoantenna in Figure 1). Moreover, we find that the interference of quadrupole and dipole radiation, even in noncentro-symmetric configurations, leads to much weaker SHG. We directly confirm these observations by measuring the emission patterns of individual nanoantennas in the back focal plane, which are distinctive for the various configurations considered. This work shows that in each investigated nanoantenna the bar element drives the nonlinear polarization while the disc elements provide the means to efficiently radiate SHG via the mutual coupling. In this sense, the 2ω-elements probe the phase of the bar's nonlinear polarization.

We investigate five different nanostructures (CI–CV) (see Figure 2a). Configurations CI and CII re-examine the concept of incorporating multiple harmonic resonances to boost SHG emission as considered in previous work.[14,25−28] Configuration CIII shows not only how to improve the polarization and dipole-like emission patterns compared to CI and CII but also highlights the importance of having the 2ω-elements radiating in phase. This is in contrast to CIV, which cancels dipole-like emission because it is centro-symmetric. Despite being noncentro-symmetric, configuration CV performs considerably worse than CIII because its quadrupole and dipole components are designed to be aligned so that they interfere. In order to fully explore the variations in SHG between the various nanoantennas

investigated, we have simulated and measured their linear extinction spectra (Figure 2b,c), their SHG spectral distribution (Figure 2d,e), and their polarization and radiation patterns (Figure 3, 4 and 5) at the second harmonic frequency. (Details of sample fabrication and the experimental setup are presented at the end of this letter.) To observe SHG in our experiments, we illuminate a single isolated nanoantenna with a near diffraction limited spot at a wavelength of 1500 nm and filter the reflected light to select only the second harmonic wavelength at 750 nm (see Figure S1). The choice to measure SHG from individual nanoantennas allows us to unambiguously assess the shape of the radiation pattern. We selected nanoantennas whose linear responses display a resonance very near the fundamental frequency, so that a similar amount of power is coupled to each nanoantenna. This will help to draw conclusions about the variations in SHG emission intensity (Figure 6).

Figure 2b,c shows the linear simulated and experimental extinction spectra of the various nanoantenna configurations under consideration (Figure 2a). The nanoantennas were designed to be doubly resonant to enhance SHG. An ω-particle is resonant near the pump wavelength of 1500 nm and due to its bar shape only scatters the pump beam when it is polarized along the x-direction. Meanwhile the 2ω-particles, resonant near 750 nm, are discs and may scatter SHG with an arbitrary polarization dependent upon their coupling with the bar. Indeed, Figure 2d,e shows that strong SHG signal emerges with a y-polarization, perpendicular to the bar, only for the doubly resonant configurations (CII to CV in Figure 2e). It is weakest for the bar alone (CI), as shown in the inset of Figure 2e. The dominance of y-polarized SHG in the doubly resonant nanoantennas reaffirm the role of the 2ω-particles in promoting SHG. In contrast, x-polarized SHG (Figure 2d) from the nanoantennas CII, CIV, and CV are comparable to the SHG of the bar alone (CI), and CIII has a suppressed response. We also note that SHG decreases by over 3 orders of magnitude for a y-polarized pump (perpendicular to the bar, see Figure S3), confirming the pivotal role of the nanoantennas' resonant modes in producing SHG.

The importance of antenna symmetry is immediately apparent when comparing the larger signal from CIII with that of CIV, shown in Figure 2e. Remarkably, even the CII nanoantenna with only a single 2ω-particle has a 2-fold improved response over CIV. It is noteworthy, however, that CIV has a distinctive distribution of SHG compared to the bar alone, CI, even though they are both centro-symmetric. Moreover, despite being noncentro-symmetric, CV has performance comparable to CIV. Symmetry arguments alone cannot provide insight into such observations, which is why a microscopic point of view is warranted. Indeed, we propose that the variation observed here stems from the interference of the SHG radiation from constituent particles within the antenna. The phase of the nonlinear polarization in the bar must determine the scattering phase of 2ω-particles within a nanoantenna and thus the SHG radiation pattern and polarization. While numerous works have considered SHG in doubly resonant nanoantennas,[11,14,25−28] configurations involving multiple 2ω-particles have not been examined before, yet could be important for creating an effective nonlinear response.

Let us now consider in more detail the characteristics of SHG emission from the various nanoantenna configurations. First, we consider the simplest CI and CII geometries, where other works on doubly resonant nanoantennas for SHG have left-off.[11,14,25−28] Figure 3a,b shows the direction of emission in
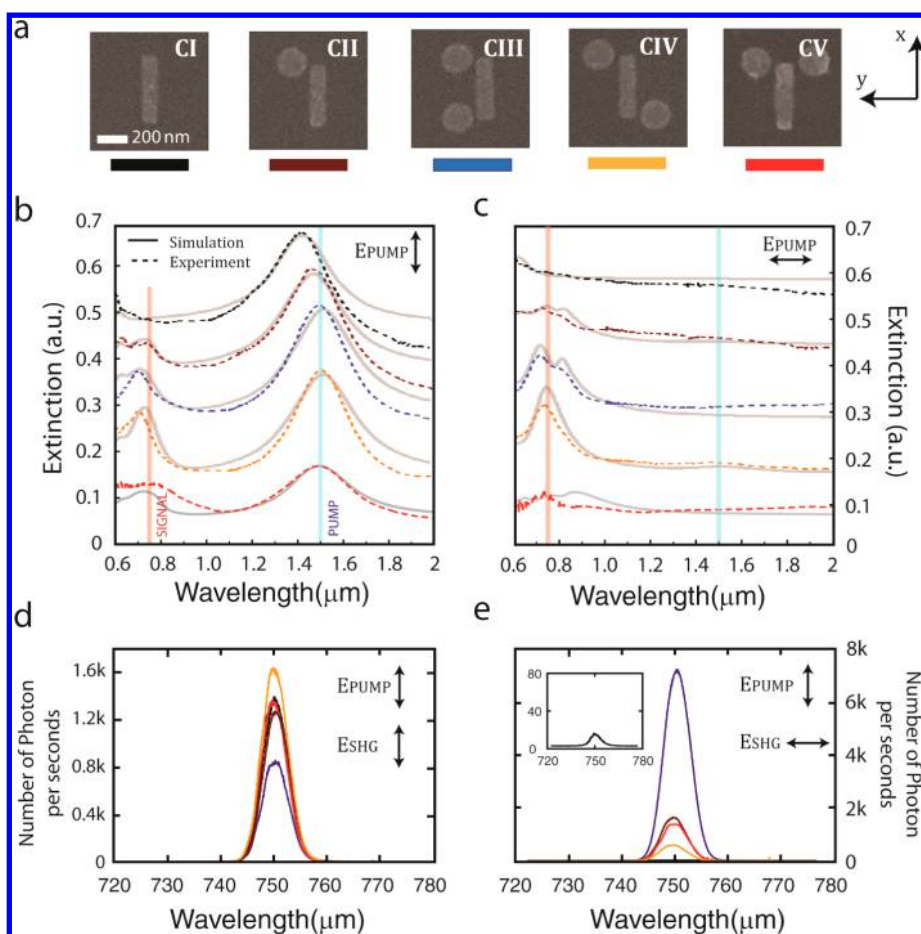
Figure 2. Linear extinction spectra and SHG of multiresonant gold nanoantennas. (a) SEM images of the five nanoantenna configuration (CI–CV) considered in this work. Dimensions of the bars are $340 \times 80 \times 40$ nm in x, y, and z, respectively, while discs are the same thickness with diameters of 160 nm. The gaps between the discs and the bar are 20 nm for all cases. (b,c) The measured (broken color lines) and simulated (solid gray lines) extinction spectra for light incident parallel (x-axis) and perpendicular (y-axis) to the bar-particle, respectively (see Note 1 of Supporting Information). (d,e) The measured SHG signals from the five configurations for a pump polarized along the bar. In d (respectively e), the SHG signal is polarized along (respectively perpendicular to) the bar. Inset of e is the SHG spectra of CI. The data have been calibrated to take into account the polarization sensitivity of the spectrometer (see Figure S2).

the back focal plane (BFP) of our microscope. We can see that the bar nanoantenna's (CI) SHG is from a dark quadrupole-like mode[29,30] (Figure 3a). Because the linear polarizability of this particle is along the x-direction, negligible y-polarized SHG is recorded. For CII, which includes a single 2ω-particle, a bright dipole-like response emerges (Figure 3b) on top of the dark quadrupole response of the bar. The bright emission is of a similar strength as the dark emission as it changes completely the polarization of SHG observed in the far field, as shown in Figure 3c,d. Meanwhile, the total dark emission is about the same in both CI and CII, as shown in Figure 2e, explaining the doubling of CII's SHG signal. Because much of the dark emission is inaccessible at normal incidence,[31] the main advantage of the 2ω-particle is to increase the directionality of SHG.

We now consider geometries CIII, CIV, and CV with two 2ω-particles, shown in Figure 4. Here CIII has 2ω-particles along the long side of the bar, CIV has them arranged on opposite sides and CV has them arranged along the short side of the bar. In the case of CIII (Figure 4a), y-polarized dipole emission constructively interferes to create brighter and more directional emission normal to the sample surface compared to CII (Figure 3b). Meanwhile, dipole emission is completely canceled in CIV (Figure 4b) as both x- and y-polarizations have a dark response.

This implies that the 2ω-particles in CIV scatter SHG out of phase leading to a 4-fold suppression of SHG compared to CIII. Differences between these nanoantennas also show up clearly in the polarization response (Figure 4d,e). While CIII is highly y-polarized from the dominant "bright" SHG from the 2ω-particles (Figure 4d), CIV has no preferred polarization with comparable x- and y-polarized "dark" emission (Figure 4e). Because CV is noncentro-symmetric (Figure 4c,f), the two dipoles interfere constructively for x-polarization, whereas they interfere destructively for y-polarization as seen by the quadrupole emission in Figure 4c. For x-polarization, the dipole interferes with the quadrupole SHG from the bar, which leads to an asymmetric radiation pattern.

In order to gain a deeper understanding of the microscopic viewpoint of CIII, CIV, and CV, we have modeled the emission of SHG using a multiple dipole model to reproduce their observed back focal plane emission patterns and polarizations (see Figure S4 and Note 3). We model the structure by interfering dipoles and a quadrupole, in which the interplay of the various phases and scattering strengths reproduces the observed data. The plasmonic modes of the structure at the second harmonic frequency are described by linear coupled Lorentzian oscillators,[32] such that each disc is represented by a dipole of field
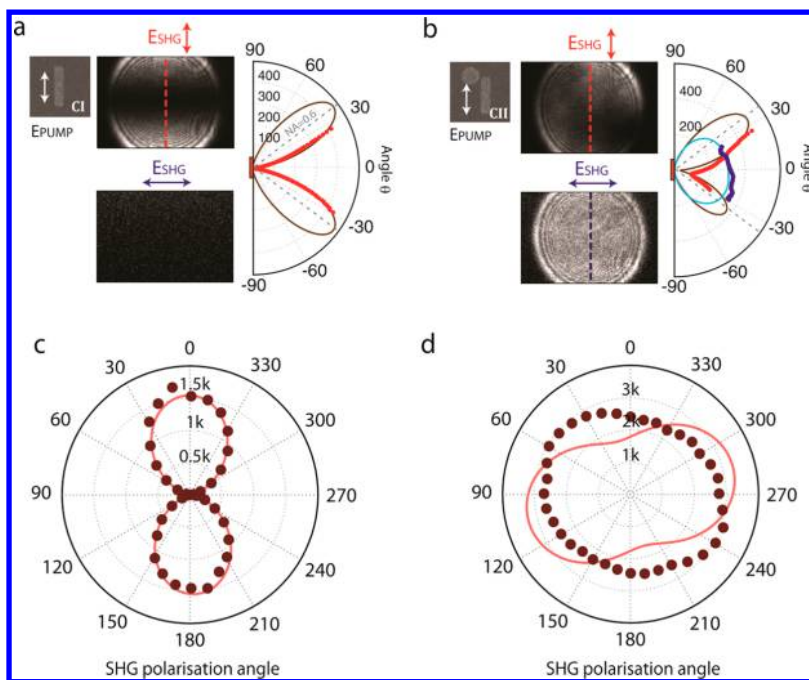
Figure 3. SHG radiation patterns and polarizations for nanoantennas CI and CII. (a,b) The direction of SHG emission for CI and CII, respectively, measured in the back focal plane of our microscope. Red (respectively blue) dots are the smoothened experimental vertical line-scan data from the *x*-(respectively *y*-) polarized back focal plane images. Brown (respectively cyan) lines are the best fit to a multipole model (see Note 3 and Figure S4 of Supporting Information for model details). Units are photon counts over 75 s integration time. (c,d) The measured (dots) and fitted (solid line) emission polarization for CI and CII, respectively. Units are total photons per second. The data have been calibrated to take into account the polarization sensitivity of the spectrometer (see Figure S2).
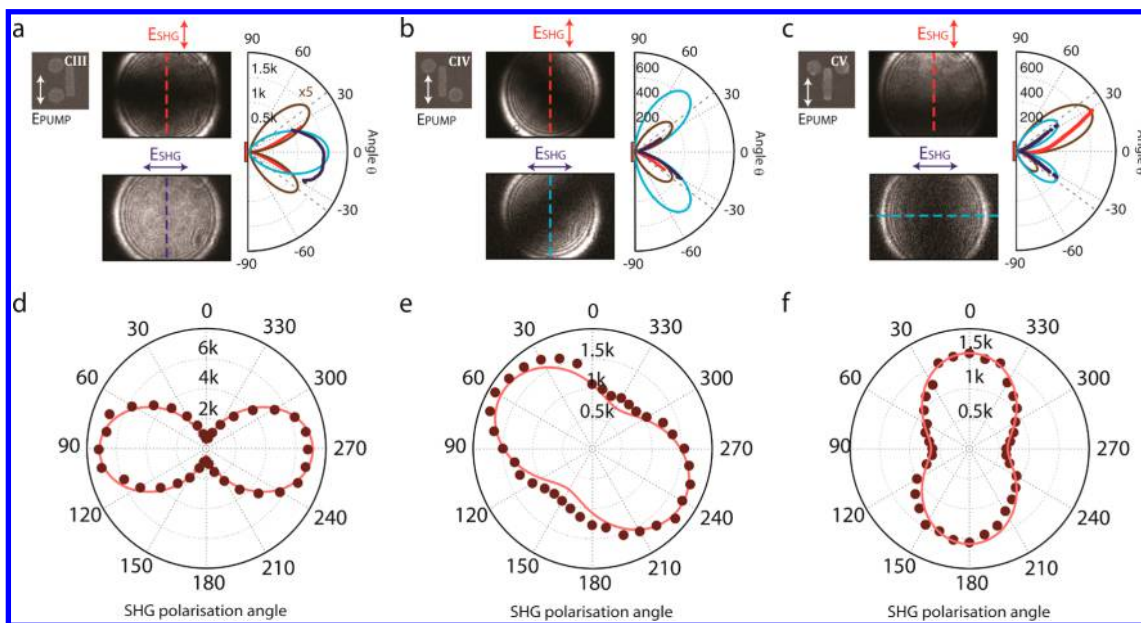
Figure 4. SHG radiation patterns and polarizations for nanoantennas CIII, CIV, and CV incorporating two 2ω-particles. (a–c) The direction of SHG emission for CIII, CIV and CV, respectively, measured in the back focal plane of our microscope. Red (respectively blue) dots are the smoothened experimental vertical line-scan data from the *x*-(respectively *y*-) polarized back focal plane images. Brown (respectively cyan) lines are the best fit to a multipole model (see Note 3 and Figure S4 of Supporting Information). Units are photon counts over 75 s integration time. (d–f) The measured (dots) and fitted (solid line) emission polarizations for CIII, CIV, and CV, respectively. Units are total photons per second. The data have been calibrated to take into account the polarization sensitivity of the spectrometer (see Figure S2).

amplitude, a_d, resonance frequency, ω_d, and loss rate, γ_d, which couples independently to the quadrupole mode of the bar of field amplitude, a_q, resonance frequency, ω_q, and loss rate, γ_q. The coupled system is then described by the inhomogeneous coupled equations with a source term, σ_q, such that

$$\begin{pmatrix} \delta_d + i\gamma_d & 0 & C \\ 0 & \delta_d + i\gamma_d & C \\ C & C & \delta_q + i\gamma_q \end{pmatrix} \begin{pmatrix} a_{d1} \\ a_{d2} \\ a_q \end{pmatrix} = \begin{pmatrix} 0 \\ 0 \\ \sigma_q \end{pmatrix}$$

(1)
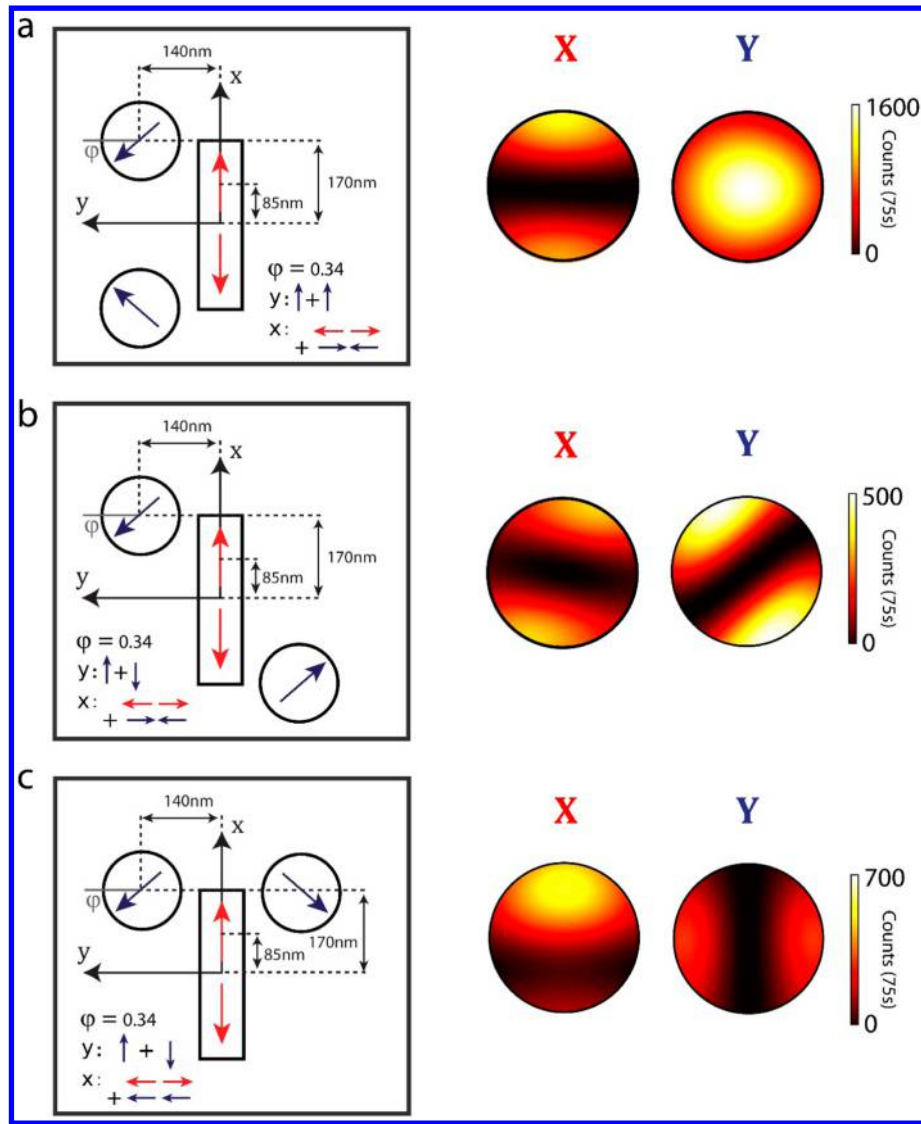
Figure 5. Dipole orientations of the antenna CIII−CV. Dipole and quadrupole orientations (left) obtained by the model required to generate the observed emission pattern and polarization (right) for (a) CIII (cf. Figure 4a), (b) CIV (cf. Figure 4b), and (c) CV (cf Figure 4c). ϕ_d is the angle between the y-axis and the disc dipole orientation. Panels on the right show the model fits to the back focal plane images in units of photon counts over 75 s integration time.

where $\delta_d = \omega - \omega_d$ and $\delta_q = \omega - \omega_q$ are the respective detunings of dipole and quadrupole modes and C is the coupling rate between the bar and the disc modes. Here, we have assumed that the nonlinear source of SHG is negligible in the discs compared to that of the bar, σ_q, because only the bar is resonant with the fundamental pump wavelength at $\lambda = 1,500$ nm. The field amplitudes of each mode are thus given by

$$\begin{pmatrix} a_{d1} \\ a_{d2} \\ a_q \end{pmatrix} = \frac{C\sigma_q}{2C^2 + \frac{\gamma_d \gamma_q}{\cos\psi_d \cos\psi_q} e^{-i(\psi_d + \psi_q)}} \begin{pmatrix} 1 \\ 1 \\ -i\frac{\gamma_d}{C}\frac{e^{-i\psi_d}}{\cos\psi_d} \end{pmatrix}$$

(2)

where the phases of dipoles and quadrupole are given by $\tan(\psi_{d/q}) = \delta_{d/q}/\gamma_{d/q}$. We note that on resonance, the quadrupole of the bar radiates $\pi/2$ out of phase with the dipole of the disc and any additional detuning of the resonance of the disc adds an extra phase shift, ψ_d, which is one of the fitting parameters in our model. The far field intensity of the antenna at a position r, is

found from the electric field contributions of one or two dipoles, $a_{di}\mathbf{E}_{di}(r - s_{di}, \phi_{di})$, $i \in \{1, 2\}$ and a quadrupole, $a_q\mathbf{E}_q(r - s_q, \phi_q)$, at positions, $s_{di/q}$, and orientations, $\phi_{di/q}$ in the x−y plane of the antenna,

$$|\mathbf{E}_T(r)|^2 = |a_{d1}\mathbf{E}_{d1}(r - s_{d1}, \phi_{d1}) + a_{d2}\mathbf{E}_{d2}(r - s_{d2}, \phi_{d2})$$
$$+ a_q\mathbf{E}_q(r - s_q, \phi_q)|^2$$

(3)

The field distributions, $\mathbf{E}_{d/q}(\mathbf{r})$, for each interfacial dipole are described by Engheta's formula,[23,33] for a substrate refractive index, $n = 1.5$. (See Supporting Information file for details of the model.) Using Jones matrices with the formula given in eq 3 the model is simultaneously fit to the x- and y-polarized back focal plane emission pattern data as well as the polarization data. The full set of parameters (see Note 3) required include the dipole positions and orientations as well as their relative phases and amplitudes, as summarized in the Table 1. We note that the quadrupole orientation $\phi_q = 0$ by definition.
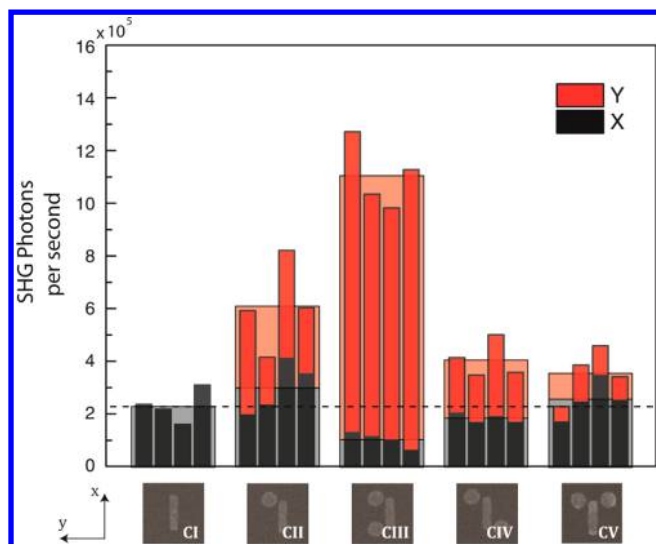
Figure 6. Contribution of *x*- and *y*-polarization to the total SHG emission for the five nanoantennas considered in this work. Large (respectively small) histograms are the mean (respectively individual) values over four distinct nanoantennas of the same configuration.

This model recreates accurately the observed emission patterns (back focal plane) and polarizations for CI–CV (see Figures 3 and 4 and Figure S4.) The calculated parameters in each configuration from the model show fairly uniform amplitudes of quadrupoles in the range of 95–110 and dipoles in the range of 45–60. This indicates that the SHG produced by each particle within these antennas is relatively uniform and that the relative performance of each antenna is mainly due to the interference of the various radiation sources.

The simulated multipole positions and orientations for CIII, that generate the correct back focal plane response as shown in Figure 4a, are shown in Figure 5a. Along the *y*-polarization, the two dipoles are in phase leading to constructive interference. Moreover, for the *x*-polarization the two dipoles are out of phase, and interfere destructively with the quadrupole to reduce the bar's quadrupolar SHG emission, which is consistent with our observations in Figure 2d,e. In contrast, Figure 5b shows the simulated multipole positions and orientations for the CIV nanoantenna that generate the correct back focal plane response as shown in Figure 4b. Since both *x*- and *y*-polarizations are quadrupolar in nature, the two dipoles must be out of phase. Finally, in the configuration CV the two dipoles are out of phase for the *y*-polarization; however, for the *x*-polarization the two in-phase dipoles interfere with the quadrupole of the bar, leading the tilted back focal plane response observed.

It is noteworthy that the modes of CIII–CV that emit the SHG are comprised of disc modes coupled to the second order mode of the bar, which produces the quadrupolar SHG of nanoantenna

CI (Figure 3a). Therefore, the characteristics of a nanoantenna's SHG can be determined by a straightforward consideration of the symmetries of the various modes at 2ω. Additional calculations and simulations of the electromagnetic fields at the nanoantenna's ω and 2ω resonances in the Supporting Information corroborate this observation (see Figure S5 and Note 2). The optimum arrangement of 2ω-particles around the bar requires a matching of the scattering phase determined by the nonlinear surface polarization, which is the source of SHG.

Figure 6 summarizes these results by showing the contributions of the *x*- and *y*-polarized SHG emission from all of the nanoantennas investigated in this work. Because the quadrupolar emission is polarized along *x*, the *y*-polarized emission shows the contribution from the discs. We can confirm that the addition of a single 2ω-particle (CII) increases the proportion of bright (dipole) emission into the *y*-polarization. Moreover, multiple 2ω-particles increase dipolar emission further but only in the configurations where they radiate in phase (CIII). Notably, configurations with multiple 2ω-particles can also reduce the SHG emission from the bar (CIII and CIV) due to residual out of phase dipole components along the *x*-direction (along the bar). Interestingly, despite being noncentro-symmetric, the CV SHG intensity is similar to a centro–symmetric structure CIV, because the dipole components interfere with the quadrupole slightly out of phase, which causes the antenna to radiate away from normal incidence.

While it could be argued that the origin of these differences, observed in Figure 6, might also come from the tiny variation in the gaps between these nanostructures,[34] relatively minor variations between repeated measurements over multiple nanoantennas of a single sample with the same lithographic exposure and from various samples were observed. This is partly because we have used 20 nm gaps between particles, which has a high reproducibility in our nanofabrication. We also note the nanoantennas CIII–CV show less antenna–antenna and sample–sample variation compared to CII, which was the most sensitive. Essentially, the variations in SHG intensity due to gap variations were minor in comparison to the variations observed due to the different configurations used.

In this article, we have introduced a range of multiresonant nanoantenna configurations that reveal the interplay of symmetry and scattering phase in SHG emission from metal nanostructures. While other works have highlighted the role of symmetry and field enhancement in antenna-driven SHG, here we identify the relevance of dipole–quadrupole interference and scattering phase in producing highly polarized and efficient SHG. In order to maximize SHG emission in multiresonant antennas, it is important to ensure an internal phase matching of an antenna's resonant elements for directional dipolar emission with a well-defined polarization. While this seems to be equivalent to requiring a noncentro-symmetric antenna, this is not a general

Table 1. Model Fitting Parameters for the Five Nanoantenna Configurations Considered in This Work[a]

	CI	CII	CIII	CIV	CV
a_q	95	105	95	105	110
a_d	N/A	47	53	44	59
ϕ_{d1}	N/A	$\pi/2 + 0.34$	$\pi/2 + 0.34$	$\pi/2 + 0.34$	$\pi/2 + 0.34$
ϕ_{d2}	N/A	N/A	$\pi/2 - 0.34$	$3\pi/2 + 0.34$	$-\pi/2 - 0.34$
a_q/a_d	N/A	2.23	1.79	2.39	1.86
ψ_d	N/A	0.41	0.62	0.7	0.6

[a]Note that ϕ_{di} were fixed to comparable values for all antennas. See Note 3 for more details.

rule. From a microscopic viewpoint, the interference of bright dipole and dark quadrupole sources within an antenna can drastically modify the SHG efficiency. The efficiency of SHG for a single nanoantenna in configuration CIII was found to be η_{SHG} > 4×10^{-7} W^{-1}, which corresponds to an effective $|\chi_{eff}^{(2)}|$ > 40 pm V^{-1} (See Note 4). We envisage that arrays of such multiresonant nanoantennas with strong dipole−active normal incidence SHG emission could allow highly effective exploitation of designer second order nonlinear optical processes within compact device settings.

Methods. *Nanoantenna Nanofabrication.* The nanoantennas were fabricated by electron beam lithography on a fused silica substrate. First, the substrate was coated with a positive resist (PMMA) and was baked at ∼180 °C for 120 s. Then the nanoantennas were defined by an electron beam exposure, followed by a development procedure. Subsequently, a 1.5 nm thick Cr film was deposited by e-beam evaporation on the substrate (to increase the Au adhesion) followed by 40 nm Au film. Lift-off and oxygen plasma were the last steps of fabrication. Linear spectroscopic characterization of the fabricated nanoparticle arrays were carried out with a Bruker Hyperion 2000 Fourier transform infrared (FTIR) microscope installed with a 36×, NA = 0.5 metallic reflective objective. The extinction (1-transmission) spectra were obtained by normalizing the transmittance curve from an array-encapsulated area with a reference spectrum taken from a bare area in close proximity to the array. Spectra were obtained in the ranges 500−1100 and 1100−2000 nm using a silicon detector and Peltier cooled InGaAs detector, respectively.

Optical Setup. For the nonlinear SHG measurements, the structure was pumped by nominally >200 fs pulses at 1500 nm, generated by the signal from a Coherent-APE Chameleon OPO, seeded by a Coherent Chameleon Ultra II. The laser was filtered by a 1000 nm cut off long pass filter (FELH1000 from Thorlabs) to suppress any lower wavelengths from the oscillator. A Dichroic mirror (DMLP1180) selectively transmits (T = 95%) the 1500 nm pump onto the sample and reflects (R = 95%) the emitted SHG toward the entrance slit of a spectrometer (Acton2300) with a detection efficiency of 28%. After the sample, the pump is rejected by 1000 nm cut off short pass (FESH1000) and 750 nm bandpass filters (Fb750-10-1, T = 60%). For all our measurement, our microscope objective is a Nikon S Plan Fluor ELWD 40× 0.6NA (T_{1500} = 30%, T_{750} = 84%) (see Figure S1). The NA of our objective allows us to collect about 26% of any uniform forward surface scattering (approximately 2.8 times more light is scattered backward in the substrate[33]). The input polarization of the pump is rotated via an achromatic half-wave plate 1100−2000 nm. The output polarization of the SHG is selected via a linear polarizer (LPVIS100-MP2), which has an extinction ratio of 10^6 at 750 nm. Four extra lenses were included in the beam paths (T = 72%): two lenses to correct for chromatic aberrations and two lenses to image the back focal plane. To maintain consistency, our intensity and back focal plane measurements were done within the same setup. In all of our measurements, we used pump powers at least an order of magnitude below the damage threshold of the nanoantennas (∼10 mW average power). Given the transmittance of the various components of our optical setup, the SHG detection efficiency is estimated to be 0.4% (see Note 4).

■ ASSOCIATED CONTENT

ⓢ Supporting Information

The Supporting Information is available free of charge on the ACS Publications website at DOI: 10.1021/acs.nanolett.6b02485.

> Further details on the experiment, sample characterization, numerical simulation, and calculation (PDF)

■ AUTHOR INFORMATION

Corresponding Author
*E-mail: r.oulton@imperial.ac.uk.

Author Contributions
S.D.G. and M.R. contributed equally to this work.

Notes
The authors declare no competing financial interest.

■ ACKNOWLEDGMENTS

■ REFERENCES

(1) Novotny, L.; Van Hulst, N. F. *Nat. Photonics* **2011**, *5* (2), 83−90.
(2) Shalaev, V. M. *Nat. Photonics* **2007**, *1* (1), 41−48.
(3) Soukoulis, C. M.; Wegener, M. *Nat. Photonics* **2011**, *5* (9), 1−8.
(4) Lapine, M.; Shadrivov, I. V.; Kivshar, Y. S. *Rev. Mod. Phys.* **2014**, *86* (3), 1093−1123.
(5) Zheludev, N. I.; Kivshar, Y. S. *Nat. Mater.* **2012**, *11* (11), 917−924.
(6) Li, G.; Chen, S.; Pholchai, N.; Reineke, B.; Wong, P. W. H.; Pun, E. Y. B.; Cheah, K. W.; Zentgraf, T.; Zhang, S. *Nat. Mater.* **2015**, *14* (6), 607−612.
(7) Lee, J.; Tymchenko, M.; Argyropoulos, C.; Chen, P.-Y.; Lu, F.; Demmerle, F.; Boehm, G.; Belkin, M. A.; Amann, M.; Alù, A.; Belkin, M. A. *Nature* **2014**, *511* (7507), 65−69.
(8) Segal, N.; Keren-Zur, S.; Hendler, N.; Ellenbogen, T. *Nat. Photonics* **2015**, *9* (3), 180−184.
(9) Aouani, H.; Rahmani, M.; Navarro-Cía, M.; Maier, S. A. *Nat. Nanotechnol.* **2014**, *9* (4), 290−294.
(10) Metzger, B.; Schumacher, T.; Hentschel, M.; Lippitz, M.; Giessen, H. *ACS Photonics* **2014**, *1* (6), 471−476.
(11) Celebrano, M.; Wu, X.; Baselli, M.; Großmann, S.; Biagioni, P.; Locatelli, A.; De Angelis, C.; Cerullo, G.; Osellame, R.; Hecht, B.; Duò, L.; Ciccacci, F.; Finazzi, M. *Nat. Nanotechnol.* **2015**, *10* (5), 412−417.
(12) Navarro-Cia, M.; Maier, S. a. *ACS Nano* **2012**, *6* (4), 3537−3544.
(13) Grinblat, G.; Rahmani, M.; Cortés, E.; Caldarola, M.; Comedi, D.; Maier, S. A.; Bragas, A. V. *Nano Lett.* **2014**, *14* (11), 6660−6665.
(14) Metzger, B.; Gui, L.; Fuchs, J.; Floess, D.; Hentschel, M.; Giessen, H. *Nano Lett.* **2015**, *15* (6), 3917−3922.
(15) O'Brien, K.; Suchowski, H.; Rho, J.; Salandrino, A.; Kante, B.; Yin, X.; Zhang, X. *Nat. Mater.* **2015**, *14* (4), 379−383.
(16) Utikal, T.; Zentgraf, T.; Paul, T.; Rockstuhl, C.; Lederer, F.; Lippitz, M.; Giessen, H. *Phys. Rev. Lett.* **2011**, *106* (13), 1−4.
(17) Pendry, J. B. *Science (Washington, DC, U. S.)* **2008**, *322* (5898), 71−73.
(18) Rose, A.; Smith, D. R. *Opt. Mater. Express* **2011**, *1* (7), 1232−1243.
(19) Zeuner, F.; Muldarisnur, M.; Hildebrandt, A.; Förstner, J.; Zentgraf, T. *Nano Lett.* **2015**, *15* (6), 4189−4193.
(20) Rodrigo, S. G.; Harutyunyan, H.; Novotny, L. *Phys. Rev. Lett.* **2013**, *110* (17), 1−5.
(21) Butet, J.; Martin, O. J. F. *Opt. Express* **2014**, *22* (24), 29693−26707.

(22) Thyagarajan, K.; Butet, J.; Martin, O. J. F. *Nano Lett.* **2013**, *13* (4), 1847−1851.

(23) Gennaro, S. D.; Sonnefraud, Y.; Verellen, N.; Van Dorpe, P.; Moshchalkov, V. V.; Maier, S. A.; Oulton, R. F. *Nat. Commun.* **2014**, *5* (4748), 3748.

(24) Czaplicki, R.; Mäkitalo, J.; Siikanen, R.; Husu, H.; Lehtolahti, J.; Kuittinen, M.; Kauranen, M. *Nano Lett.* **2015**, *15* (1), 530−534.

(25) Aouani, H.; Navarro-Cia, M.; Rahmani, M.; Sidiropoulos, T. P. H.; Hong, M.; Oulton, R. F.; Maier, S. A. *Nano Lett.* **2012**, *12* (9), 4997−5002.

(26) Thyagarajan, K.; Rivier, S.; Lovera, A.; Martin, O. J. F. *Opt. Express* **2012**, *20* (12), 12860−12865.

(27) Czaplicki, R.; Husu, H.; Siikanen, R.; Mäkitalo, J.; Kauranen, M.; Laukkanen, J.; Lehtolahti, J.; Kuittinen, M. *Phys. Rev. Lett.* **2013**, *110*, 093902.

(28) Harutyunyan, H.; Volpe, G.; Quidant, R.; Novotny, L. *Phys. Rev. Lett.* **2012**, *108* (21), 217403.

(29) Dadap, J. I.; Shan, J.; Heinz, T. F. *J. Opt. Soc. Am. B* **2004**, *21* (7), 1328−1347.

(30) Bachelier, G.; Russier-Antoine, I.; Benichou, E.; Jonin, C.; Brevet, P. *J. Opt. Soc. Am. B* **2008**, *25* (6), 955.

(31) Celebrano, M.; Savoini, M.; Biagioni, P.; Adam, P.; Duò, L.; Cerullo, G.; Finazzi, M. *Phys. Rev. B: Condens. Matter Mater. Phys.* **2009**, *80*, 2−5.

(32) Zhang, S.; Genov, D. A.; Wang, Y.; Liu, M.; Zhang, X. *Phys. Rev. Lett.* **2008**, *101*, 1−4.

(33) Engheta, N.; Papas, C. H.; Elachi, C. *Radio Sci.* **1982**, *17* (6), 1557−1566.

(34) Black, L.-J.; Wiecha, P. R.; Wang, Y.; de Groot, C. H.; Paillard, V.; Girard, C.; Muskens, O. L.; Arbouet, A. *ACS Photonics* **2015**, *2* (11), 1592−1601.